

# Improving axial resolution in SIM using deep learning

Boland, Miguel; Cohen, Edward A. K.; Flaxman, Seth; Neil, Mark

September 4, 2020

## Abstract

Structured Illumination Microscopy is a widespread methodology to image live and fixed biological structures smaller than the diffraction limits of conventional optical microscopy. Using recent advances in image up-scaling through deep learning models, we demonstrate a method to reconstruct 3D SIM image stacks with twice the axial resolution attainable through conventional SIM reconstructions. We further evaluate our method for robustness to noise & generalisability to varying observed specimens, and discuss potential adaptations of the method to further improvements in resolution.

## 1 Introduction

Structured Illumination Microscopy (SIM) is a super-resolution technique which enables a two-fold increase in lateral resolution (X/Y axis, perpendicular to the line of sight of the microscope) when compared to conventional fluorescence microscopy [7] [5]. SIM functions through the illumination of structured light onto a specimen in varying angles and phases to construct a stack of images, the ensemble of which contains a wider spectral range of frequencies than obtained via a single exposure. Image stacks are then reconstructed into a single super-resolved image using computational algorithms. A wide range of illumination patterns can be used, including 3D patterns that allow for improvements in axial resolution (Z axis, parallel to line of sight of the microscope) [9]. This has proven to be a useful investigative tool for the analysis of live biological processes as it avoids most sample damage traditionally associated with electron microscopy [3]. Example applications include in-vivo imaging of synapses in mice [15], or analysing the distribution of proteins on chromosomes, a task previously unfeasible due to the relative scale of the protein and a confocal microscope's diffraction limit [17]. As such, the further improvement of image reconstruction methodologies for microscopy may allow the observation of previously unobserved live biological processes.

Improvements in axial resolution have historically been achieved by advances in optical setup and illumination techniques, such as 3D-SIM [6], TIRF-SIM [23], spot-scanning SR-SIM [22] or 2-photon SR-SIM [8]. As these techniques can incur significant costs and complexity, recent developments in deep learning have been adapted and optimised to address these issues from a purely computational approach. Proposed deep learning methods for SIM have successfully demonstrated reductions in aberrations and reconstruction artifacts due to movements of the specimen or low-light conditions [1] [10] [11], but as of yet, deep learning networks have not been applied to the problem of reconstructing SIM image stacks to a resolution beyond that attainable by standard SIM methodologies. Training a network to take as its input a set of SIM images as might be produced by a 2D-SIM microscope setup (2-beam, 3-angle) and with a target that has the resolution characteristics of a 3D-SIM microscope, would allow the network to achieve an axial resolution comparable to 3D SIM microscopes without the motion artifacts or photo-bleaching caused by high image counts [2].

Building on the work of deep learning networks applied to SIM reconstructions, a modified RCAN [24] deep neural net is trained to reconstruct SIM image stacks at double the axial resolution than that attainable via the original SIM reconstruction methodology [5]. Simulated training and test data is generated from both dense and biologically realistic 3D point clouds, at both standard resolution (SR) and high resolution (HR) as detailed in section 2. The network is evaluated against test data to investigate the method’s effectiveness at resolving structures composed of point illuminations (section 3). Further analysis is performed that demonstrates robustness to low-lighting conditions (section 3). Limitations in network generalisability and broader potential of the work is discussed in section 4.

## 2 Methods

### 2.1 Deep learning

#### 2.1.1 Existing work

Deep learning has been applied to SIM reconstruction with varying goals, such as accelerating the imaging process by reducing the required number of raw frames and inferring the spectral information which is no longer imaged. This has been achieved using U-Nets [10] and CycleGAN (a variation of a Conditional Generative Adversarial Network) [11]. These diverge from our goal which is to attain a higher axial resolution whilst maintaining a  $2\times$  increase in lateral resolution. Image super-resolution for generic photography has progressed considerably in the past decade, resulting in a large variety of architectures and techniques [19]. Notably, these form paradigms regarding the pre or post upsampling of inputs (relative to convolutional or other image processing), methods of image interpolation, residual learning, network recursiveness or parallel paths in addition to a large number of architecture-specific features.

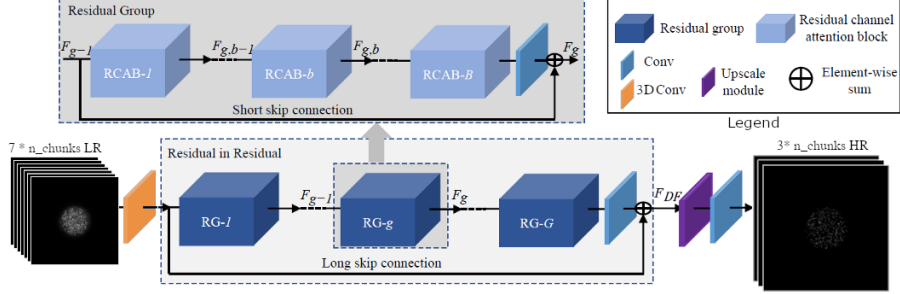


Figure 1: Modified RCAN network architecture, adapted from [24]. Note the use of a 3D convolution at the input, and the use of a single input channel and 3 output channels.

Amongst these exists the Recursive Channel Attention Network (RCAN) [24], which is engineered to use inter-channel features (RGB colors in the original network) in addition to sub-pixel upsampling. These are particularly suited to SIM reconstruction, as this process entails the recombination of multiple raw images (i.e channels) into an up-scaled image. An RCAN for SIM reconstruction was successfully trained using simulated SIM stacks of generic stock imagery [1], which forms the basis for our architecture.

### 2.1.2 Network architecture

The network architecture is based on the RCAN [24] which was previously used to implement a form of SIM reconstruction without up-scaling [1]. We modified the network to re-implement the up-scaling module found in the original implementation, therefore doubling the lateral output image size. Furthermore, the first 2D convolutional layer was replaced by a 3D convolution in order to infer information from other SIM stacks within the same processing chunk (see section below for chunk-generating procedure) prior to higher order operations (which take place in the residual blocks of the network). The number of output channels was also changed according to the chunk size, such that 3 consecutive gray scale (i.e. single channel) images were produced for every inputted SIM stack.

### 2.1.3 Chunk processing

Input SIM stacks were processed in chunks to allow varying depths of image stacks to be compatible with the network and improve the model’s performance by inferring relations between consecutive axial images. In this scheme, a chunk size of two corresponds to a network input of 14 images (7 frames per SIM image \* 2 chunk size) and a network output of 6 frames (3 frames per SIM image \* 2 chunk size). Chunk size was determined experimentally by modifying

the training data and input channels for the architecture described in section 2; these were then evaluated using 24 withheld chromatin structure images and a series of images of spherical point clouds with increasing point densities.

The chunk size had no significant effect on the network’s MSE (Mann-Whitney U-Test,  $p < 0.05$  for all pairs of chunked data), but the Structural Similarity Index (SSIM, a comparative metric of conservation of structural information between an image and reference image [25]) was higher for a chunk size of 3 (U-Test,  $p < 0.05$  for 6/9 comparisons). This indicates that a chunk size of 3 maximises the conservation of the structure of the images, as reflected by the mean lateral FWHM (smaller than all other chunk size’s means, U-Test,  $p < 0.05$ ) and axial mean (smaller than all other chunk sizes, U-Test,  $p < 0.05$ ).

#### 2.1.4 Data pre & post processing

Pairs of SIM image stacks and HR confocal images were axially sliced to produce chunked sets of images as described above. As the simulated images extended beyond the simulated underlying data, image pairs with little signal (mean pixel value below  $5 \times 10^{-7}$ ) were discarded. The remaining set of chunked images was then normalised to a range of  $[0-1]$ .

Negative pixel values did occur in the RCAN outputs due to small normally distributed random errors in output values; as a majority of test images are zero-valued backgrounds, many of the errors cause small negative values. The output was therefore post-processed to truncate negative values, which is in effect the equivalent to using an additional *reLu* layer on the network but without causing a loss of learning gradient.

#### 2.1.5 Training methodology

All deep learning models were implemented using the PyTorch library (version 1.5) [12] in Python 3.7. Models were trained for 300 epochs with an MSE loss function and a training/validation data split of 90/10. The starting learning rate was set to  $10^{-6}$ , was adjusted if the validation rate plateaued during training through the use of the *ReduceLROnPlateau* method provided by PyTorch, and a further 1% decrease was applied every 5 epochs to ensure fine tuning in later epochs. Network gradients were clipped at  $\pm 0.1$  to avoid exploding gradients. Training / validation sets were drawn from all generated data except for withheld test cases, which were randomly selected prior to training. Training took approximately 8 hours on a set of 2 Nvidia GTX 2080 TI GPUs.

## 2.2 Data simulation

The model was trained using simulated SIM image stacks as input, and an up-sampled confocal image as ground truth. The methods used to generate these and benchmark SIM reconstructions are described below.

### 2.2.1 SIM image stacks

Raw SIM images were generated from 3D point cloud data; these simulated a biologically realistic chromatin structure [18] or a point cloud encompassed in a sphere with varying numbers of point emitters. The simulated microscope utilised a 7-frame setup based on the interference of 3 coherent beams to produce a 2D hexagonal illumination pattern on the sample; this is well illustrated in Figure 2 D-F of Ingerman et. al., 2019 [9]. The structured illumination is assumed to be achieved using a light-sheet arrangement [14] thereby avoiding the issues of reduced resolution enhancement usually found with this SIM geometry in an epi-illumination setup. The system was simulated with a camera size of 256x256 pixels of size 6.5  $\mu\text{m}$  square, an objective magnification of 60, with a numerical aperture of 1.1 and an illumination/emission wavelength of 525 nm. The structured illumination is assumed to be achieved using a light-sheet geometry [14]. Photobleaching and other image quality degradation were not simulated as part of the experiment, though low-lighting conditions were simulated using Poisson statistics.

### 2.2.2 High-resolution confocal microscope simulation

Target output stacks were generated using a simulation of a confocal microscope on the same cloud point data. The parameters of the microscope were simulated to out-perform the simulated SIM microscope (halved pixel size, illumination wavelength is divided by  $\sqrt{2}$ , axial & lateral nyquist sampling rate doubled, squared PSF function). These parameters ensure a doubling in both axial and lateral resolutions.

The number of output frames was also increased from 40 to 120 frames in order to improve the precision of measurements of axial resolution.

### 2.2.3 SIM reconstructions

While complete high resolution images can be reconstructed with a set of just 7 images, this hexagonal patterned SIM illumination reconstructs according to the same carrier spatial frequencies as are found in a 2-beam, 3-angle setup using 9-frames [7] [5]. As a consequence the processing of the 7-frame data to a super-resolved image with enhanced lateral resolution [4] was achieved in a similar way to the standard SIM reconstruction algorithm [5]. Reconstructed SIM images were calculated to provide a comparative baseline for our RCAN-reconstructed images. This was implemented using Matlab (see section 5), and was modified to output 120 frames to match the number of output frames in our high resolution confocal simulations and network outputs.

## 2.3 Measuring resolution

The Full Width at Half Maximum (FWHM) metric has commonly been used to evaluate the resolution of microscopy images [6] [20]. It is defined as the width of a waveform at half the peak intensity; a large FWHM would indicate a wider

point spread function (PSF) resulting in a less detailed image, whilst a smaller FWHM reflects a narrower PSF and a sharper image.

The FWHM was estimated using a method using auto-correlation functions [16], thereby evaluating the FWHM for every point light source in an image rather than individually and manually selected data points. The auto-correlation function (ACF) of an image was calculated using the inverse Fourier transform of the power spectrum on individual 3D datasets. As cross-correlation of signal from neighbouring light point sources is present in dense test cases, it is removed by modelling the image auto-correlation as the sum of two Gaussians, one representing the auto-correlation of individual PSFs in the images and the second representing the cross-correlation between different, randomly distributed PSFs. These are estimated using a bounded Least-Squares regression, and the FWHM is calculated from the Gaussian with the smallest standard deviation. An example of the modelling process is illustrated in supplementary materials A4. The Python & Scipy implementation of this methodology is available via GitHub, and an equivalent mathematical notation is available in the supplementary materials Section A1.

### 3 Results

#### 3.1 Doubling axial resolution using RCAN networks

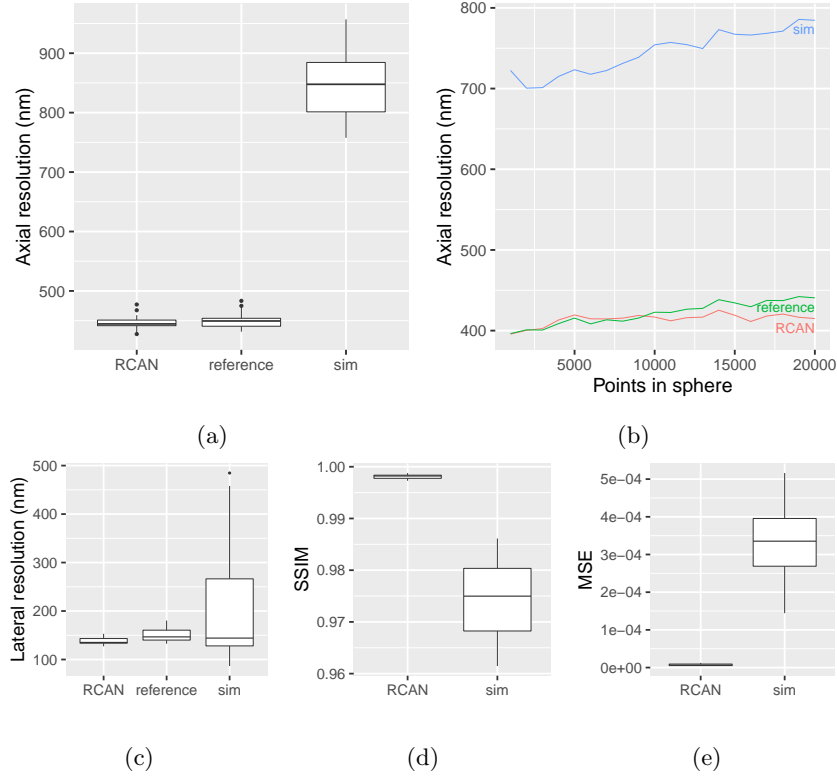


Figure 2: The proposed deep learning model (see section 2) demonstrates a doubled axial resolution compared to a standard SIM reconstruction when evaluated against 24 simulated chromatin structures (a) (whiskers represent percentiles, boxes represent IQR). An equivalent improvement in resolution is observed when reconstructing images of point clouds of increasing densities (b). Lateral resolution is maintained when compared to SIM reconstructions (c). Finally the RCAN (mean=0.998, std=0.0004) appears to better conserve the structure of the underlying data compared to SIM (mean=0.974, std=0.007) as measured by SSIM [25] (T-test  $t(24)=23.158$ ,  $p<0.005$ ) whilst also reducing the MSE (RCAN (mean=7.36e-06, std=2.55e-06), SIM (mean=3.39e-04, std=9.57e-05), T-test  $t(24)=16.07$ ,  $p<0.005$ ).

The network’s ability to double the axial resolution was tested using 24 unseen simulated chromatin structures; this is visible in Figure 2a. The mean axial Full Width at Half Maximum (FWHM) for RCAN reconstructions (mean=445.96nm, std=11.8) was found to be significantly smaller than those produced using SIM

(mean=844.27nm, std=50.57) (T-Test  $t(24)=37.576$ ,  $p<0.005$ ). We further found the model to be robust to increasing point density when compared to standard SIM reconstructions (see Figure 2b). This is achieved without significantly affecting the lateral resolution (X & Y axis, perpendicular to line of sight of the microscope), as seen in Figure 2c, and maintaining a strong conservation of structure as seen in Figure 2d. This is illustrated by the orthogonal Y/Z view in the supplementary material - Figure A2, where the high structural fidelity and low background noise of the RCAN output contrasts with the SIM reconstruction.



### 3.2 Robustness in low-light imaging conditions

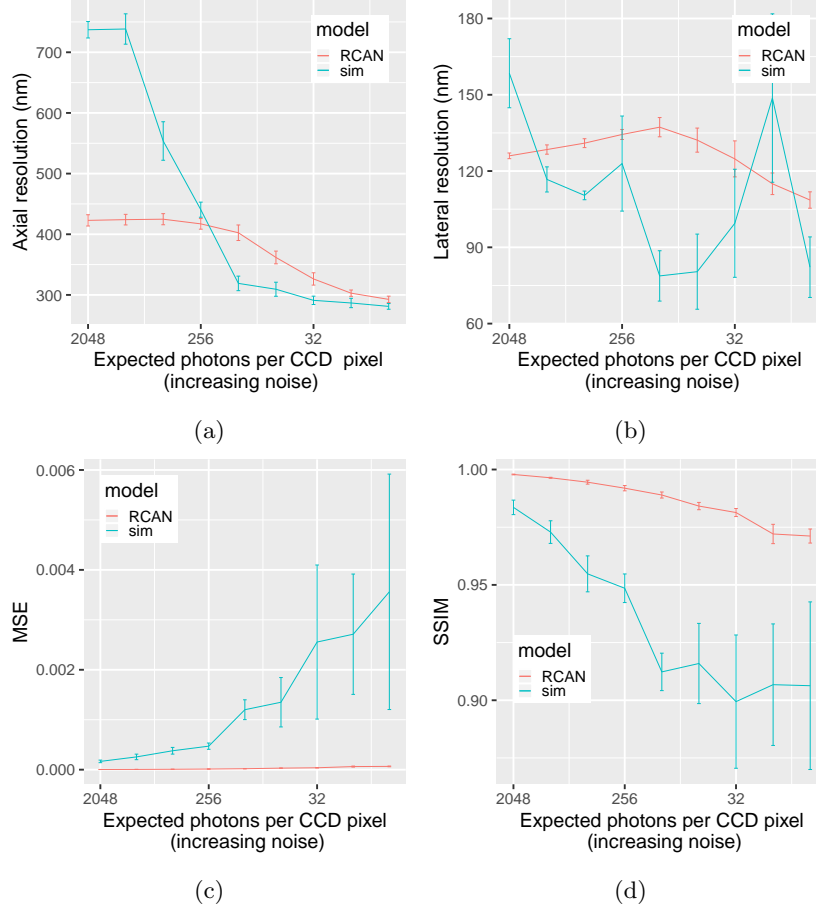


Figure 3: Effect of Poisson noise on quality of image reconstruction, run on 5 different simulated chromatin structures with 9 levels of Poisson noise. Error bars illustrate the standard error. The RCAN network provides more stable axial and lateral resolutions (see figures a and b) without a major loss in image quality compared to SIM reconstructions, as shown by the divergence in MSE and SSIM (see figures c and d).

An additional dataset was generated using 4 other simulated chromatin structures tainted with Poisson noise. The signal-to-noise ratio was decreased by reducing the expected photons per camera CCD pixel, thereby simulating low-lighting conditions. The RCAN model demonstrated robustness against low-lighting conditions by maintaining a consistent axial resolution (Figure 3a) MSE (Figure 3c) and SSIM [25] (Figure 3d), in contrast to the reconstructed SIM

images which diverge from the reference HR images in SSIM and MSE in worsening lighting conditions. The notable decrease in axial resolution for SIM reconstructions at lower lighting levels is due to a breakdown in the quality of the reconstruction, as reflected by the large increase in MSE and decrease in SSIM, whilst these are more consistent for RCAN reconstructions.

### 3.3 Evaluation against third party data

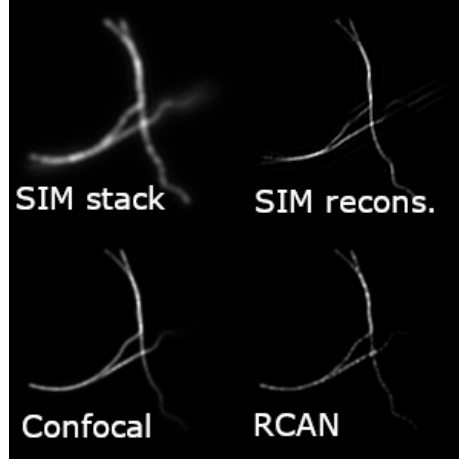


Figure 4: Frame 35 of the simulated MT1.N1.HD SMLM dataset [13]; simulated SIM stack (top-left), SIM-reconstructed stack (top-right), high-res confocal image (bottom-left) and RCAN output (bottom-right). Note the high structural fidelity and sharpness of the RCAN reconstruction, without the presence of faint side-lobe artifacts seen in the SIM reconstruction. These are visible as duplicate chromatin microtubules shifted on either side of the well illuminated structure, and are more apparent in the full video of the image stacks (available in the supplementary material).

The training data examined above differs from the biological structures observed in other SIM experiments, such as actin filaments [10], membranes [1] or other biological structures which form wider continuous illuminations. To evaluate our network’s performance on data containing these structures, cloud point data for Single Molecule Localisation Microscopy (SMLM) was taken from a SMLM competition’s training dataset [13] (training sets MT1.N1.LD ( $\approx 8\,000$  points, low-density) and MT1.N1.HD ( $\approx 13\,000$  points, high-density)). These contain shallow and narrow filament structures with high point densities, allowing us to evaluate the generalisability of our method to biological structures observed in other studies. SIM image stacks and high-resolution confocal images were simulated from this data, and processed by the RCAN network. As visualised in Figure 4, the RCAN (bottom-right) was able to produce the expected microtubule without the side-lobe artifacts seen in the SIM image; these are visible

as faint duplicate microtubules on either side of a well illuminated strand, and are more distinguishable to non-expert viewers through the video provided in the supplementary material. The difference in axial resolution (RCAN mean: 331.4nm, SIM mean: 605.1nm, reference HR confocal mean: 372.9nm) reflected the previous test on chromatin data, as did the similarity in lateral resolution (RCAN: 170.8nm, SIM: 165.7nm, reference: 172.8nm), mse (RCAN: 1.6e-05, SIM: 4.4e-05) and SSIM (RCAN: 0.998, SIM: 0.996).

### 3.4 Execution time

The execution time of our RCAN model was measured by computing SIM reconstructions of large image stacks. Reconstruction of 24 image stacks (280 frames each, i.e 40 SIM images with 7 frames per image) was repeated 10 times, allowing us to mitigate any file system interference due to shared use of the compute server. PyTorch’s *DataParallel* module enables the distribution of image chunks from the same image stack to an array GPU computation units, thereby further accelerating the reconstruction of a 3D image stack. A mean execution time of 0.69 seconds per image stack was demonstrated using a shared GPU cluster of two Nvidia GeForce RTX 2080 Ti. Further GPU parallelisation may be worthwhile for larger image stacks though I/O overheads allow no further performance gains for our test data.

## 4 Discussion

As demonstrated by the results in section 3, the RCAN architecture described in section 2 is capable of producing SIM reconstructions with a higher axial resolution than current 2D SIM reconstructions without a loss of lateral resolution or structural fidelity. This was demonstrated to be robust in low-light levels, which is typically a complexity of SIM and had been previously addressed by other deep-learning solutions [10].

The use of two simulated structure types in our training data (biological structures and sphere-bounded point-clouds) demonstrates some capacity for the network to generalise to varying structures in observed specimens; this was reflected by the performance of the network on simulated SMLM data in Figure 4. The task of generalising to other sources of data was addressed in varying approaches, such as training with real-world images [1]. This mitigates the likelihood of over-fitting a model to a distinct biological structure, as they are not present across all training data. In contrast, a U-Net approach found the need to re-train models to mitigate the occurrence of artifacts in reconstructed images [10]. Therefore it may be necessary to train on a wider variety of real or synthetic datasets to optimise the reconstruction of other biological structures using this method.

An issue which has yet to be addressed by image up-scaling networks is the

limits of the up-scaling factor with regards to image fidelity. The original implementation of the RCAN architecture [24] demonstrates  $4\times$  up-scaling but with a severe degradation of SSIM; this brings into question the certainty with which reconstructed images can be considered, especially if the ratio of up-scaling is further increased. The modified RCAN described here may be more effective when attempting higher ratios of up-scaling as the initial set of information contains many more frames (i.e channels) per output image, and therefore has the capacity to contain more information to be reconstructed into the HR image. A brief insight into the effect of removing one of these channels (see supplementary material A3) demonstrates the use of all channels in the reconstruction of the image, as the removal of any single image deteriorates the MSE and SSIM statistics in comparison to the reconstruction without masked layers. Ultimately, as the ratio of up-scaling goes beyond the capability of human validation, further imaging of structures via destructive methods (such as electron microscopy) could also validate final time points in reconstructed time lapse SIM images. A cross-validation could be performed using training groups formed of distinct biological structures; the sensitivity of the network to its training data would then provide better insight into potential reconstruction biases present in the network. This could further be extended by generating ensembles of trained models; this has previously been demonstrated in the use of image restoration for fluorescence microscopy [21]. In this scheme, each model would be trained on a random subset of the training data, and the output of all trained models for any given novel image reconstruction would be considered to form a statistical model for each output pixel. This could allow a degree of statistical confidence, which may be increasingly required to assert the certainty of reconstructions especially at larger ratios of image up-scaling.

## 5 Data access

All code used to generate training data, define & train deep learning models and evaluate these models is available at <https://github.com/mb1069/sim-axial-resolution>.

## 6 Funding

Funding for this project is provided by

- the European Union (under the Horizon 2020 Framework Programme: H2020 Future and Emerging Technologies (801336 - PROCHIP)).
- the Wellcome Trust’s PhD program at Imperial College, London.

## References

- [1] Charles N. Christensen, Edward N. Ward, Pietro Lio, and Clemens F. Kaminski. ML-SIM: A deep neural network for reconstruction of structured illumination microscopy images. arXiv 2003.11064, 08 2020.
- [2] Junchao Fan, Xiaoshuai Huang, Liuju Li, Shan Tan, and Liangyi Chen. A protocol for structured illumination microscopy with minimal reconstruction artifacts. *Biophysics Reports*, 5(2):80–90, Apr 2019.
- [3] Reto Fiolka, Lin Shao, E. Hesper Rego, Michael W. Davidson, and Mats G. L. Gustafsson. Time-lapse two-color 3D imaging of live cells with doubled resolution using structured illumination. *Proceedings of the National Academy of Sciences*, 109(14):5311–5315, 2012.
- [4] H Gong, W Guo, C Dunsby, and M.A.A. Neil. GPU-accelerated, real-time reconstruction in Python of three dimensional datasets from structured illumination microscopy with hexagonal patterns. *Submitted to Philosophical Transactions of the Royal Society A*, 09 2020.
- [5] M. G. L. Gustafsson. Surpassing the lateral resolution limit by a factor of two using structured illumination microscopy. *Journal of Microscopy*, 198(2):82–87, 2000.
- [6] Mats G. L. Gustafsson, Lin Shao, Peter M. Carlton, C. J. Rachel Wang, Inna N. Golubovskaya, W. Zacheus Cande, David A. Agard, and John W. Sedat. Three-dimensional resolution doubling in wide-field fluorescence microscopy by structured illumination. *Biophysical journal*, 94(12):4957–4970, Jun 2008.
- [7] Rainer Heintzmann and Christoph G. Cremer. Laterally modulated excitation microscopy: improvement of resolution by using a diffraction grating. In Irving J. Bigio, Herbert Schneckenburger, Jan Slavik, Katarina Svanberg M.D., and Pierre M. Viallet, editors, *Optical Biopsies and Microscopic Techniques III*, volume 3568, pages 185–196. International Society for Optics and Photonics, SPIE, 1999.
- [8] Maria Ingaramo, Andrew G. York, Peter Wawrzusin, Oleg Milberg, Amy Hong, Roberto Weigert, Hari Shroff, and George H. Patterson. Two-photon excitation improves multifocal structured illumination microscopy in thick scattering tissue. *Proceedings of the National Academy of Sciences*, 111(14):5254–5259, 2014.
- [9] E.A. Ingeman, R.A. London, R. Heintzmann, and M.G.L. Gustafsson. Signal, noise and resolution in linear and nonlinear structured-illumination microscopy. *Journal of Microscopy*, 273(1):3–25, 2019.

- [10] Luhong Jin, Bei Liu, Fenqiang Zhao, Stephen Hahn, Bowei Dong, Ruiyan Song, Timothy C. Elston, Yingke Xu, and Klaus M. Hahn. Deep learning enables structured illumination microscopy with low light levels and enhanced speed. *Nature Communications*, 11(1):1934, Apr 2020.
- [11] Chang Ling, Chonglei Zhang, Mingqun Wang, Fanfei Meng, Luping Du, and Xiaocong Yuan. Fast structured illumination microscopy via deep learning. *Photonics Research*, 8(8):1350–1359, Aug 2020.
- [12] Adam Paszke, Sam Gross, Francisco Massa, Adam Lerer, James Bradbury, Gregory Chanan, Trevor Killeen, Zeming Lin, Natalia Gimelshein, Luca Antiga, Alban Desmaison, Andreas Kopf, Edward Yang, Zachary DeVito, Martin Raison, Alykhan Tejani, Sasank Chilamkurthy, Benoit Steiner, Lu Fang, Junjie Bai, and Soumith Chintala. Pytorch: An imperative style, high-performance deep learning library. In H. Wallach, H. Larochelle, A. Beygelzimer, F. d'Alché-Buc, E. Fox, and R. Garnett, editors, *Advances in Neural Information Processing Systems 32*, pages 8024–8035. Curran Associates, Inc., 2019.
- [13] Daniel Sage, Thanh-An Pham, Hazen Babcock, Tomas Lukes, Thomas Pengo, Jerry Chao, Ramraj Velmurugan, Alex Herbert, Anurag Agrawal, Silvia Colabrese, Ann Wheeler, Anna Archetti, Bernd Rieger, Raimund Ober, Guy M. Hagen, Jean-Baptiste Sibarita, Jonas Ries, Ricardo Henriques, Michael Unser, and Seamus Holden. Super-resolution fight club: assessment of 2D and 3D single-molecule localization microscopy software. *Nature Methods*, 16(5):387–395, May 2019.
- [14] Federico Sala, Michele Castriotta, Petra Paiè, Andrea Farina, Sarah D’Annunzio, Alessio Zippo, Roberto Osellame, Francesca Bragheri, and Andrea Bassi. High-throughput 3d imaging of single cells with light-sheet fluorescence microscopy on chip. *Biomedical Optics Express*, 11(8):4397–4407, Aug 2020.
- [15] Raphaël Turcotte, Yajie Liang, Masashi Tanimoto, Qinrong Zhang, Ziwei Li, Minoru Koyama, Eric Betzig, and Na Ji. Dynamic super-resolution structured illumination imaging in the living brain. *Proceedings of the National Academy of Sciences*, 116(19):9586–9591, 2019.
- [16] Sarah L. Veatch, Benjamin B. Machta, Sarah A. Shelby, Ethan N. Chiang, David A. Holowka, and Barbara A. Baird. Correlation functions quantify super-resolution images and estimate apparent clustering due to overcounting. *PLOS ONE*, 7(2):1–13, 02 2012.
- [17] Chung-Ju Rachel Wang, Peter M. Carlton, Inna N. Golubovskaya, and W. Zacheus Cande. Interlock formation and coiling of meiotic chromosome axes during synapsis. *Genetics*, 183(3):905–915, 2009.
- [18] Siyu Wang, Jinbo Xu, and Jianyang Zeng. Inferential modeling of 3D chromatin structure. *Nucleic Acids Research*, 43(8):54, 02 2015.

- [19] Zhihao Wang, Jian Chen, and Steven C.H. Hoi. Deep learning for image super-resolution: A survey. *IEEE Transactions on Pattern Analysis and Machine Intelligence*, 2020.
- [20] Eva Wegel, Antonia Göhler, B. Christoffer Lagerholm, Alan Wainman, Stephan Uphoff, Rainer Kaufmann, and Ian M. Dobbie. Imaging cellular structures in super-resolution with sim, sted and localisation microscopy: A practical comparison. *Scientific Reports*, 6(1):27290, Jun 2016.
- [21] Martin Weigert, Uwe Schmidt, Tobias Boothe, Andreas Müller, Alexandr Dibrov, Akanksha Jain, Benjamin Wilhelm, Deborah Schmidt, Coleman Broaddus, Siân Culley, Mauricio Rocha-Martins, Fabián Segovia-Miranda, Caren Norden, Ricardo Henriques, Marino Zerial, Michele Solimena, Jochen Rink, Pavel Tomancak, Loic Royer, Florian Jug, and Eugene W. Myers. Content-aware image restoration: pushing the limits of fluorescence microscopy. *Nature Methods*, 15(12):1090–1097, Dec 2018.
- [22] Andrew G. York, Sapun H. Parekh, Damian Dalle Nogare, Robert S. Fischer, Kelsey Temprine, Marina Mione, Ajay B. Chitnis, Christian A. Combs, and Hari Shroff. Resolution doubling in live, multicellular organisms via multifocal structured illumination microscopy. *Nature Methods*, 9(7):749–754, Jul 2012.
- [23] L. J. Young, F. Ströhl, and C. F. Kaminski. A Guide to Structured Illumination TIRF Microscopy at High Speed with Multiple Colors. *Journal of Visualised Experiments*, 111(111), 05 2016.
- [24] Yulun Zhang, Kunpeng Li, Kai Li, Lichen Wang, Bineng Zhong, and Yun Fu. Image super-resolution using very deep residual channel attention networks. In Vittorio Ferrari, Martial Hebert, Cristian Sminchisescu, and Yair Weiss, editors, *Computer Vision – ECCV 2018*, pages 294–310, Cham, 2018. Springer International Publishing.
- [25] Zhou Wang, A. C. Bovik, H. R. Sheikh, and E. P. Simoncelli. Image quality assessment: from error visibility to structural similarity. *IEEE Transactions on Image Processing*, 13(4):600–612, 2004.

# Improving axial resolution in SIM using deep learning - supplementary material

Boland, Miguel; Cohen, Edward A. K.; Flaxman, Seth; Neil, Mark

September 4, 2020

## 1 Supplementary material A1 - Measuring FWHM

As detailed in the main paper, the FWHM is measured from the autocorrelation function using the methodology below. The example details the estimation of the axial (Z) resolution; lateral resolution can be calculated by summing over the Z axis in Equation 3, selecting the zero-padded row of matrix F in Equation 5 which contains the peak value for the matrix and decomposing the series into two Gaussian functions in Equation 6.

Let  $I$  be a 3D microscopy  $X * Y * Z$  image stack of dimensions  $(N_X, N_Y, N_Z)$

Let

$$P = |FFT_3(I)|^2 \text{ where } FFT_3 \text{ is a 3D fast-Fourier transform.} \quad (2)$$

Summing  $P$  across the  $X$  and  $Y$  dimensions gives vector  $S$  with  $k$ th element

$$S_k = \sum_{i=1}^{N_X} \sum_{j=1}^{N_Y} P_{i,j,k}. \quad (3)$$

We then pad vector  $S$  using the following rule

$$S_k = \begin{cases} S_k & \text{if } k < \frac{N_Z}{2} \\ 0 & \text{if } \frac{N_Z}{2} < k < \frac{N_Z}{2} + p \\ S_{k-p} & \text{if } k > \frac{N_Z}{2} + p, \end{cases} \text{ where } p \text{ corresponds to the width of 0-padding.} \quad (4)$$

We then inverse FFT this vector

$$F = FFT_{shift}(IFFT(S)), \quad (5)$$

and decompose it into two Gaussian functions  $g_{acf}(\alpha, \mu, \sigma)$  and  $g_{ccf}(\alpha, \mu, \sigma)$ , for the auto-correlation and cross-correlation function, respectively, via a least squares fit

$$F = g_{acf}(\alpha_{acf}, \mu_{acf}, \sigma_{acf}) + g_{ccf}(\alpha_{ccf}, \mu_{ccf}, \sigma_{ccf}). \quad (6)$$



Constraints are placed that  $\mu_{acf} \approx \mu_{ccf}$  and  $\sigma_{acf} < \sigma_{ccf}$ . The FWHM is then measured on  $g_{acf}(\alpha_{acf}, \mu_{acf}, \sigma_{acf})$ .

## 2 Supplementary material A2 - Y/Z cross sections of output images

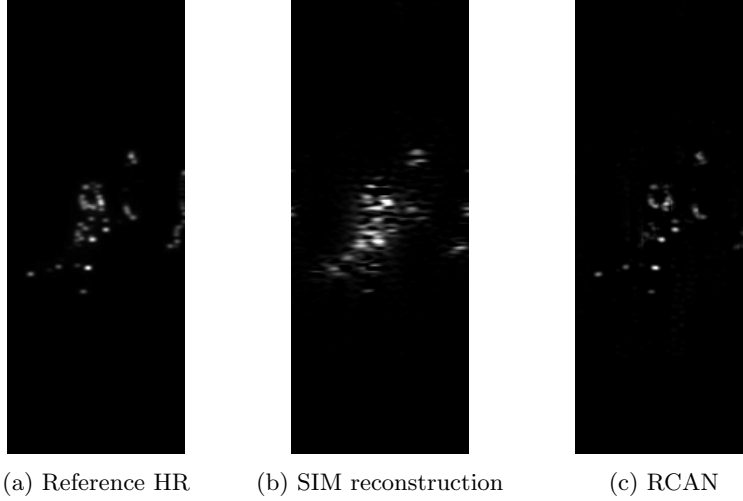


Figure 1: Y/Z cross-sections of a simulated chromatin structure

## 3 Supplementary material A3 - Effect of obscuring a frame from the RCAN's input

The charts below demonstrate the effect of pinning any individual SIM frame to 0 when inputting a chunk of 3 SIM reconstructions into the RCAN. This demonstrates the usage of all available input frames to reconstruct the output image, as the lowest MSE and best SSIM are only achieved when no frame is obscured.

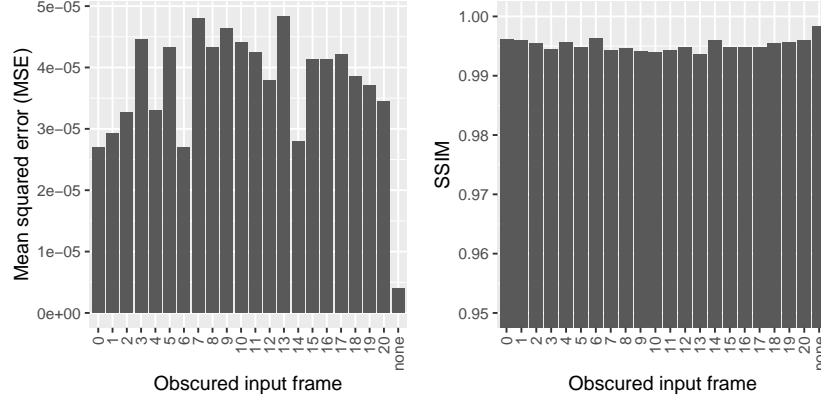


Figure 2: Evaluating the effect of masking one of 21 frames in an image chunk, taken from a simulated chromatin structure & processed by our model.

#### 4 Supplementary material A4 - Example modelling of autocorrelation function as sum of two gaussians

Figure 3 illustrates modelling of the inverse FFT of an image stack’s power spectrum, as described in Section A1. *Gauss1* is modelled as the autocorrelation function, whilst *Gauss2* models the cross-correlation function; the sum of both model the measured function well as demonstrated by the *Gauss1+Gauss2* series.

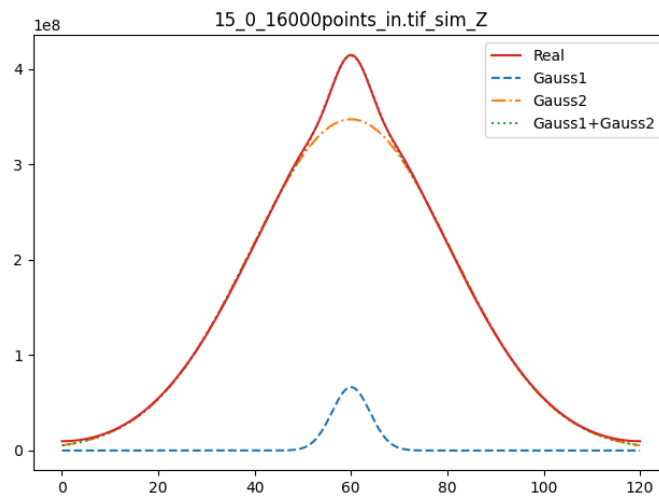


Figure 3: Decomposing an image stack's inverse FFT of the power spectrum into the sum of two Gaussians